PAPER

Check for updates

DFT screening of dual-atom catalysts on carbon nanotubes for enhanced oxygen reduction reaction and oxygen evolution reaction: comparing dissociative and associative mechanisms†

Xiangyi Zhou, [ID] [a] Mohsen Tamtaji, [ID] [b] Weijun Zhou, [ID] [c] William A. Goddard III [ID] *[d] and GuanHua Chen [ID] *[ab]

Dual-atom catalysts (DACs) are promising for the oxygen reduction reaction (ORR) and the oxygen evolution reaction (OER). However, two vital factors, namely curvature effects and dissociative mechanisms, are often overlooked in DAC studies, which may miss the possibility of finding the most promising candidates. To provide a mechanistic understanding of the role of these two essential factors in effective electrocatalyst design, we explore systematically the catalytic potential of $MM'N_6$-DACs supported on graphene and single-walled carbon nanotubes (CNTs) with two diameters within both dissociative and associative mechanisms where M and M′ represent Fe, Co, Ni, Cu, Ru, Rh, Pd, or Pt metals. More than ten DACs have shown high activity with overpotential lower than that of common commercial catalysts, notably non-precious $CoCuN_6$-DACs exhibiting extremely low ORR overpotential of 0.09 V_{RHE} and low OER overpotential of 0.10 V_{RHE}, and bifunctional ORR and OER overpotential of 0.22 V_{RHE}. We find that CNT substrates strengthen the adsorption of intermediates on $CoCuN_6$-DACs compared to graphene substrates, due to increased electronic density of states of metal atoms near the Fermi level. The dissociative mechanism circumvents the constraints of scaling relationship in the associative mechanism, so that several DACs favoring the dissociative mechanism exhibit substantially improved activity, with lower overpotential than the theoretical minimum of the associative mechanism. These results not only shed light on designing high-performance catalysts for the ORR and OER but also deepen the theoretical understanding of the catalytic mechanism and curvature effects on DACs.

1. Introduction

The Oxygen Reduction Reaction (ORR) and the Oxygen Evolution Reaction (OER) involving transformations between water and oxygen, are crucial for (rechargeable) metal–air batteries, fuel cells, and electrolyzers.[1–6] In particular, in the oxygen electrode of rechargeable metal–air batteries, both reactions are important. These sluggish reactions require catalysts to boost their rate.[7] Currently, popular commercial catalysts for the ORR and OER are based on bulk Pt[8,9] and RuO_2,[10,11] respectively, which are hampered by their high cost and only medium

[a]Department of Chemistry, The University of Hong Kong, Pokfulam Road, Hong Kong SAR, China. E-mail: ghc@everest.hku.hk

[b]Hong Kong Quantum AI Lab Limited, Pak Shek Kok, Hong Kong SAR, China

[c]QuantumFabless Limited, Pak Shek Kok, Hong Kong SAR, China

[d]Materials and Process Simulation Center (MSC), MC 139-74, California Institute of Technology, Pasadena CA, 91125, USA. E-mail: wag@caltech.edu

† Electronic supplementary information (ESI) available: The formation energy and dissolution potential of all DACs, as well as adsorption free energies and overpotentials on all DACs and related SACs. See DOI: https://doi.org/10.1039/d4ta03519d

activity. Therefore, developing replacements combining economic viability with superior performance for these precious catalysts is an urgent and important challenge. In particular, bifunctional catalysts capable of catalyzing both reactions are essential for improving rechargeable metal–air batteries.

Designing atomically dispersed metal catalysts, such as single-atom catalysts (SACs)[12–18] and dual-atom catalysts (DACs),[19,20] is widely regarded as a promising strategy to replace the need for high-cost Pt and RuO_2 catalysts to achieve reliable activity and reduce cost by ultra-high metal utilization. Significant theoretical and experimental efforts have been devoted to exploring potential SACs for various electrocatalytic processes, such as the ORR,[21–26] OER,[22,25] the N_2 reduction reaction (N_2RR)[27] and the CO_2 reduction reaction (CO_2RR).[28–30] However, these reactions involve multiple intermediates, whereas the activity of SACs is severely limited by the scaling relationship between intermediates. By contrast, DACs have the potential to outperform SACs' performance due to possible synergy between two active sites.[31–33] For example, more than ten metallic dimers anchored by N-doped graphene have shown excellent OER activity, outperforming their corresponding SACs.[34]

The ORR and OER can take place through both dissociative and associative mechanisms. Most of the existing research on DACs for mono- and bi-functional oxygen electrocatalysis considers only their performance for the associative mechanism in planar configuration, without considering curvature effects or the dissociative mechanism. However, these two factors may play a key role in designing effective DACs. Studies have shown that curvature effects can be utilized to adjust the activity of SACs for various electrocatalytic reactions[35–42] and CoCo-DACs for oxygen electrocatalysis.[43] In addition, some recent studies have shown that oxygen electrocatalysis on DACs may favor a dissociative mechanism due to the synergy of dual atoms.[34,43,44] Therefore, to address the lack of DAC screening for oxygen electrocatalysis that considers curvature and dissociation, we conducted a systematic screening for mono- and bifunctional ORR/OER catalysts, incorporating these critical factors.

Herein, in the hope of finding the best DACs for oxygen electrocatalysis, we theoretically investigated the ORR and OER performance of MM′N$_6$-DACs under 3 curvature conditions for both the dissociative and associative mechanisms, where M and M′ represent Fe, Co, Ni, Cu, Ru, Rh, Pd, or Pt metals. Dual-atom sites on graphene represent the planar condition (noted as $d = \infty$ nm), while these sites on carbon nanotubes (CNTs) with two diameters (d) represent two curved conditions (*i.e.* $d = 1.3$ nm, and $d = 0.8$ nm). We found some promising catalysts for mono- and bi-functional oxygen electrocatalysis with ultra-low overpotential especially in the dissociative mechanism, such as

• CoCu$_{d=\infty \text{ nm}}$-DAC (with ORR overpotential $\eta^{\text{ORR}} = 0.09$ V, OER overpotential $\eta^{\text{OER}} = 0.13$ V, and bifunctional ORR and OER overpotential $\eta^{\text{bifunc}} = \eta^{\text{ORR}} + \eta^{\text{OER}} = 0.09 + 0.13 = 0.22$ V) and

• CoCu$_{d=1.3 \text{ nm}}$-DAC (with $\eta^{\text{ORR}} = 0.22$ V, $\eta^{\text{OER}} = 0.10$ V, and $\eta^{\text{bifunc}} = \eta^{\text{ORR}} + \eta^{\text{OER}} = 0.22 + 0.10 = 0.32$ V).

Moreover, unlike the tethered performance dictated by scaling relationships in the associative mechanism, the dissociative pathway in oxygen electrocatalysis offers a novel possibility for catalyst activity free from the above limitations. We analyze the curvature effects on the adsorption of intermediates on CoCuN$_6$-DACs and discuss the electronic origin.
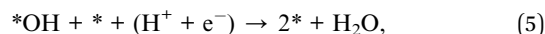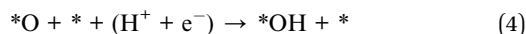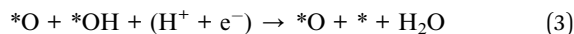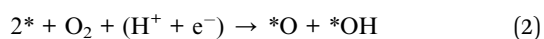
2. Methods

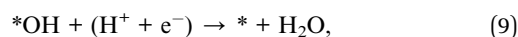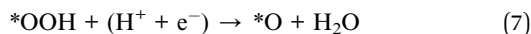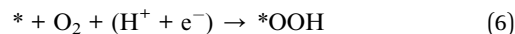### 2.1. Dissociative and associative mechanisms of the ORR and OER

The ORR involving the transfer of four electrons and protons can be expressed as follows:

$$O_2 + 4 (H^+ + e^-) \rightarrow 2H_2O \quad E° = 1.23 \text{ V} \tag{1}$$

The ORR can proceed through either a dissociative mechanism or an associative mechanism. The four steps of the dissociative mechanism can be expressed as:

$$2* + O_2 + (H^+ + e^-) \rightarrow *O + *OH \tag{2}$$

$$*O + *OH + (H^+ + e^-) \rightarrow *O + * + H_2O \tag{3}$$

$$*O + * + (H^+ + e^-) \rightarrow *OH + * \tag{4}$$

$$*OH + * + (H^+ + e^-) \rightarrow 2* + H_2O, \tag{5}$$

while those of the associative mechanism can be expressed as:

$$* + O_2 + (H^+ + e^-) \rightarrow *OOH \tag{6}$$

$$*OOH + (H^+ + e^-) \rightarrow *O + H_2O \tag{7}$$

$$*O + (H^+ + e^-) \rightarrow *OH \tag{8}$$

$$*OH + (H^+ + e^-) \rightarrow * + H_2O, \tag{9}$$

where * represents the adsorption site. The OER is regarded as the reverse reaction of the ORR.

For the dissociative mechanism, the adsorption free energies (ΔG) of intermediates were calculated as:

$$\Delta G_{*O/*OH} = G_{*O/*OH} - G_* + \frac{3}{2}G_{H_2} - 2G_{H_2O} - 3eU \tag{10}$$

$$\Delta G_{*OH/*OH} = G_{*OH/*OH} - G_* + G_{H_2} - 2G_{H_2O} - 2eU \tag{11}$$

$$\Delta G_{*OH} = G_{*OH} - G_* + \frac{1}{2}G_{H_2} - G_{H_2O} - eU. \tag{12}$$

By contrast, for the associative mechanism,

$$\Delta G_{*OOH} = G_{*OOH} - G_* + \frac{3}{2}G_{H_2} - 2G_{H_2O} - 3eU \tag{13}$$

$$\Delta G_{*O} = G_{*O} - G_* + G_{H_2} - G_{H_2O} - 2eU \tag{14}$$

$$\Delta G_{*OH} = G_{*OH} - G_* + \frac{1}{2}G_{H_2} - G_{H_2O} - eU. \tag{15}$$

The energy of $(H^+ + e^-)$ at potential U was obtained through the computational hydrogen electrode (CHE) model as $\frac{1}{2}G_{H_2} - eU$.

2.2. Computational details

All spin-polarized density functional theory (DFT) calculations were performed using VASP 5.4.4. The exchange–correlation functional was Perdew–Burke–Ernzerhof (PBE) based on the generalized gradient approximation (GGA) with a plane-wave cutoff energy of 500 eV.[45–48] Van der Waals interactions were included using the Grimme D3 method.[49,50] VASPsol was used to simulate the implicit solvation effect of water.[51,52]

A vacuum space of 15 Å was employed to avoid interactions between two adjacent periodic images for all structure models. For structural models based on graphene, the Brillouin zone was sampled with 3 × 1 × 4 and 5 × 1 × 7 k-point grids based on the Monkhorst–Pack scheme for structural optimization and single-point energy calculations, respectively. For structural

models based on carbon nanotubes, k-point grids were $1 \times 1 \times 4$ and $1 \times 1 \times 7$, respectively. The convergence thresholds for force and electronic structure energy were 0.02 eV Å^{-1} and 10^{-5} eV,[53] respectively.

For each elementary step in oxygen electrocatalysis, the computational hydrogen electrode (CHE) model was employed to compute the Gibbs free energy change (ΔG) as:[54]

$$\Delta G = \Delta E + \Delta ZPE - T\Delta Sw \quad (16)$$

here ΔE is the electronic energy difference, ΔZPE is the zero-point energy, T is the temperature (298.15 K), and ΔS is the entropy correction.

The theoretical onset potential and overpotential were calculated from ΔG of intermediates in the elementary reaction steps. In the dissociative mechanism, the onset potential of the ORR and OER was calculated as:

$$U_{ORR}^{onset} = -\max\{(\Delta G_{*O/*OH} - 4.92), (\Delta G_{*OH/*OH} - \Delta G_{*O/*OH}),$$
$$(\Delta G_{*OH} - \Delta G_{*OH/*OH}), (-\Delta G_{*OH})\}/e \quad (17)$$

$$U_{OER}^{onset} = -\max\{(4.92 - \Delta G_{*O/*OH}), (\Delta G_{*O/*OH} - \Delta G_{*OH/*OH}),$$
$$(\Delta G_{*OH/*OH} - \Delta G_{*OH}), (\Delta G_{*OH})\}/e \quad (18)$$

By contrast, in the associative mechanism, the onset potential of the ORR and OER was calculated as:

$$U_{ORR}^{onset} = -\max\{(\Delta G_{*OOH} - 4.92), (\Delta G_{*O} - \Delta G_{*OOH}),$$
$$(\Delta G_{*OH} - \Delta G_{*O}), (-\Delta G_{*OH})\}/e \quad (19)$$

$$U_{OER}^{onset} = -\max\{(4.92 - \Delta G_{*OOH}), (\Delta G_{*OOH} - \Delta G_{*O}),$$
$$(\Delta G_{*O} - \Delta G_{*OH}), (\Delta G_{*OH})\}/e \quad (20)$$

For both mechanisms, the ORR, OER and bifunctional overpotentials were calculated as[25,41]

$$\eta^{ORR} = |1.23 - U_{ORR}^{onset}| \quad (21)$$

$$\eta^{OER} = |1.23 - U_{OER}^{onset}| \quad (22)$$

$$\eta^{bifunc} = \eta^{ORR} + \eta^{OER} \quad (23)$$

3. Results and discussion

3.1. Structure and stability of DACs

Fig. 1a illustrates the structure models of studied MM′N$_6$-DACs. To simulate DACs under different curvature conditions, the planar state with zero curvature effect was represented by dual-atom sites anchored on nitrogen-doped graphene (*i.e.* $d = \infty$ nm, representing no curvature), and two curved conditions were represented by those on nitrogen-doped single-walled carbon nanotubes (CNTs) with two diameters (*i.e.* $d = 1.3$ nm representing smaller curvature, and $d = 0.8$ nm representing larger curvature).[38,41] In this way, we have covered a wide range of curvatures.

Experimentally, the planar-state DACs can be synthesized by anchoring metal dimers on a carbon substrate such as graphene[55] or porous carbon,[56] while the curved ones can be synthesized on curved carbon substrates such as CNTs.[57–59] For
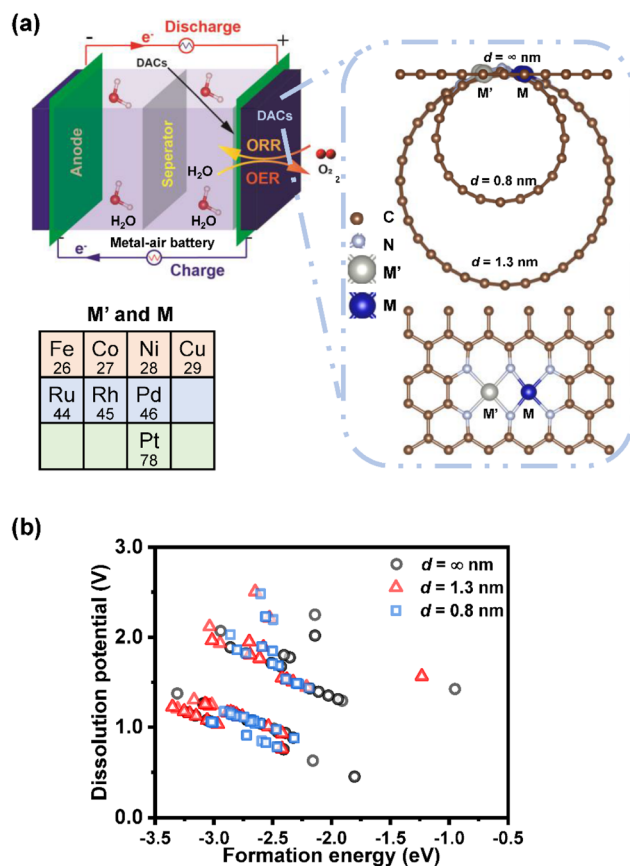

Fig. 1 Schematics and stability of studied DACs. (a) Schematics for MM′N$_6$-DACs at different curvatures for electrocatalyzing the ORR and OER. Each metallic dimer MM′ is anchored by 6 nitrogen atoms in N-doped graphene ($d = \infty$ nm) and N-doped carbon nanotubes ($d = 1.3$ nm and $d = 0.8$ nm). For each metal site, 8 transition metals are considered: Fe, Co, Ni, Cu, Ru, Rh, Pd, or Pt. Atom labels: O (red), H (pink), C (brown), N (light blue), M′ (gray) and M (dark blue). (b) Formation energy and dissolution potential of studied DACs.

example, FeCo DACs on two kinds of CNT substrates have been synthesized for ORR catalysis,[58,59] and Ni$_2$ DACs on the CNT substrate have been synthesized for electrochemical CO$_2$ reduction.[57] This indicates the feasibility of synthesizing DACs with surface curvature. In the future, more curved DACs may be synthesized, and curved DACs may be confirmed to have potential applications in OER catalysis.

For DAC models with different N species and relative positions, the stability of the model is strongly influenced by the local coordination environment of the metal dimers.[60] Here we focused on the most stable model with the lowest formation energy.[60] In this DAC model, each metal dimer is anchored by four pyridine nitrogen atoms and two amino nitrogen atoms, denoted as MM′N$_6$-DACs (or MM′-DACs for brevity). We considered 8 transition metals (Fe, Co, Ni, Cu, Ru, Rh, Pd, or Pt) for the dual-metal sites since they are common design choices for DACs for the ORR and OER.[34,55,61,62]

To examine the possibility of experimentally synthesizing these DACs and their electrochemical stability, we calculated

their formation energy (E_{form}) and dissociation potential (U_{diss}) as follows,[34,63]

$$E_{form} = (E_{DAC} - E_{N-C} - E_{M'} - E_M)/2 \quad (24)$$

$$U_{diss} = U_{diss}^0(\text{M-bulk}) - E_{form}/ne \quad (25)$$

E_{DAC} represents the total energy of the DACs and E_{N-C} is the total energy of the nitrogen-doped carbon substrate. Here $E_{M'}$ and E_M are the atomic energies of metals M and M′ in their most stable bulk state, respectively. U_{diss}^0(M-bulk) represents the standard dissolution potential of the bulk metals. And n is the number of electrons transferred during the dissolution.[34]

If $E_{form} < 0$ eV, we regard the DAC as feasible to synthesize experimentally. When $U_{diss} > 0$, we regard the DAC as electrochemically stable. Fig. 1b indicates the formation energy and dissolution potential of the DACs investigated. All proposed DACs have negative formation energies and positive dissolution potentials, suggesting that they are synthetically feasible and electrochemically stable. Tables S1–S3† list the exact values of E_{form} and U_{diss} under the three curvature conditions.

3.2. ORR and OER activity of DACs

Fig. 2 compares two mechanisms of the ORR and OER. In the ORR, O_2 is reduced to water through four steps of electron–proton transfers, which can proceed through dissociative and associative mechanisms.

The four steps of the ORR can be expressed as
- $O_2 \leftrightarrow {}^*O + {}^*OH \leftrightarrow 2{}^*OH \leftrightarrow {}^*OH \leftrightarrow H_2O$ in the dissociative mechanism
- $O_2 \leftrightarrow {}^*OOH \leftrightarrow {}^*O \leftrightarrow {}^*OH \leftrightarrow H_2O$ in the associative mechanism.

By contrast, the OER can be regarded as the reverse reaction of the ORR where water is oxidized into O_2. More details about

these two mechanisms are illustrated in Section 2.1. Most existing research on DACs considers their performance only for the associative mechanism. However, some recent studies show that oxygen electrocatalysis on DACs may instead involve the dissociative mechanism due to the synergy of the dual atoms,[34,43,44] suggesting that for DACs, the dissociative mechanism deserves more attention. Therefore, both mechanisms were considered in this study.

Fig. 3 exhibits theoretical activity, adsorption free energy and promising candidates of investigated DACs for mono- and bifunctional oxygen electrocatalysis in the two mechanisms. Adsorption free energies and overpotentials of all DACs are shown in Fig. S1 and S2,† respectively. The theoretical activity of all DACs is indicated in volcano plots (Fig. 3a–f) with the best candidates marked by stars. The Gibbs free energy diagrams of the best candidates are shown in Fig. 4a and S3.† Here lower overpotential means higher catalytic activity. The three benchmarks for screening DAC candidates for the ORR, OER, and bifunctional oxygen electrocatalysis were set as

ORR overpotential of Pt (111) (0.45 V),
OER overpotential of RuO_2 (110) (0.37 V), and
bifunctional overpotential (0.82 V), the summation of the former two values.[25]

DACs with overpotential lower than these benchmarks are potential catalysts for the corresponding reactions in the oxygen electrode of rechargeable metal–air batteries.

By comparing the activity of the best DACs for mono- and bifunctional oxygen electrocatalysis in the two mechanisms, we can see that the dissociative mechanism allows the identification of DACs with ultra-high activity, as the best DACs in the dissociative mechanism exhibit much higher activity than those in the associative mechanism. In the dissociative mechanism, the best DACs for the ORR, OER, and bi-functional oxygen electrocatalysis are

- $CoCu_{d=\infty \text{ nm}}$-DAC ($\eta^{ORR} = 0.09$ V),
- $CoCu_{d=1.3 \text{ nm}}$-DAC ($\eta^{OER} = 0.10$ V), and
- $CoCu_{d=\infty \text{ nm}}$-DAC ($\eta^{bifunc} = 0.22$ V).

as shown in Fig. 3a–c. However in the associative mechanism, the best DACs for the ORR, and OER and the two best DACs for bi-functional oxygen electrocatalysis are

- $FeCo_{d=\infty \text{ nm}}$-DAC ($\eta^{ORR} = 0.26$ V), and
- $RhFe_{d=0.8 \text{ nm}}$-DAC ($\eta^{OER} = 0.26$ V),
- $RhFe_{d=0.8 \text{ nm}}$-DAC ($\eta^{bifunc} = 0.62$ V)
- $CoNi_{d=1.3 \text{ nm}}$-DAC ($\eta^{bifunc} = 0.62$ V)

as shown in Fig. 3d–f.

To analyze whether the adsorption of intermediates conforms to the scaling relationship, a well-known bottleneck in developing high-performance oxygen electrocatalysts,[34,64] we performed linear fitting for adsorption free energies of intermediates in both mechanisms. Interestingly, for the dissociative pathway, both $\Delta G_{{}^*O/{}^*OH}$ and $\Delta G_{{}^*OH/{}^*OH}$ exhibit a poor linear relationship with $\Delta G_{{}^*OH}$, with $R^2 \sim 0.4$, as shown in Fig. 3g. This indicates that the dissociative mechanism enables DACs to circumvent the scaling relationship between intermediates, which facilitates finding DACs with ultra-high activity for mono- and bi-functional oxygen electrocatalysis.[34,43] However for the associative pathway, both $\Delta G_{{}^*OOH}$ and $\Delta G_{{}^*O}$ correlate strongly
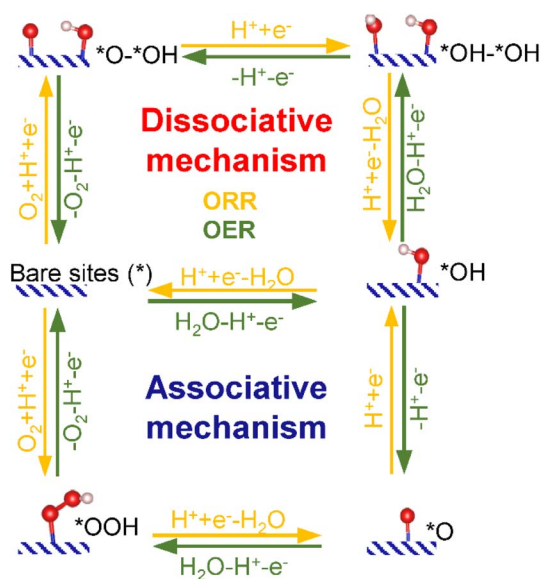

Fig. 2 Two reaction mechanisms for the ORR and OER. The yellow color represents the reaction pathway of the ORR, while the green color represents the reaction pathway of the OER.

28384 | *J. Mater. Chem. A*, 2024, **12**, 28381–28389

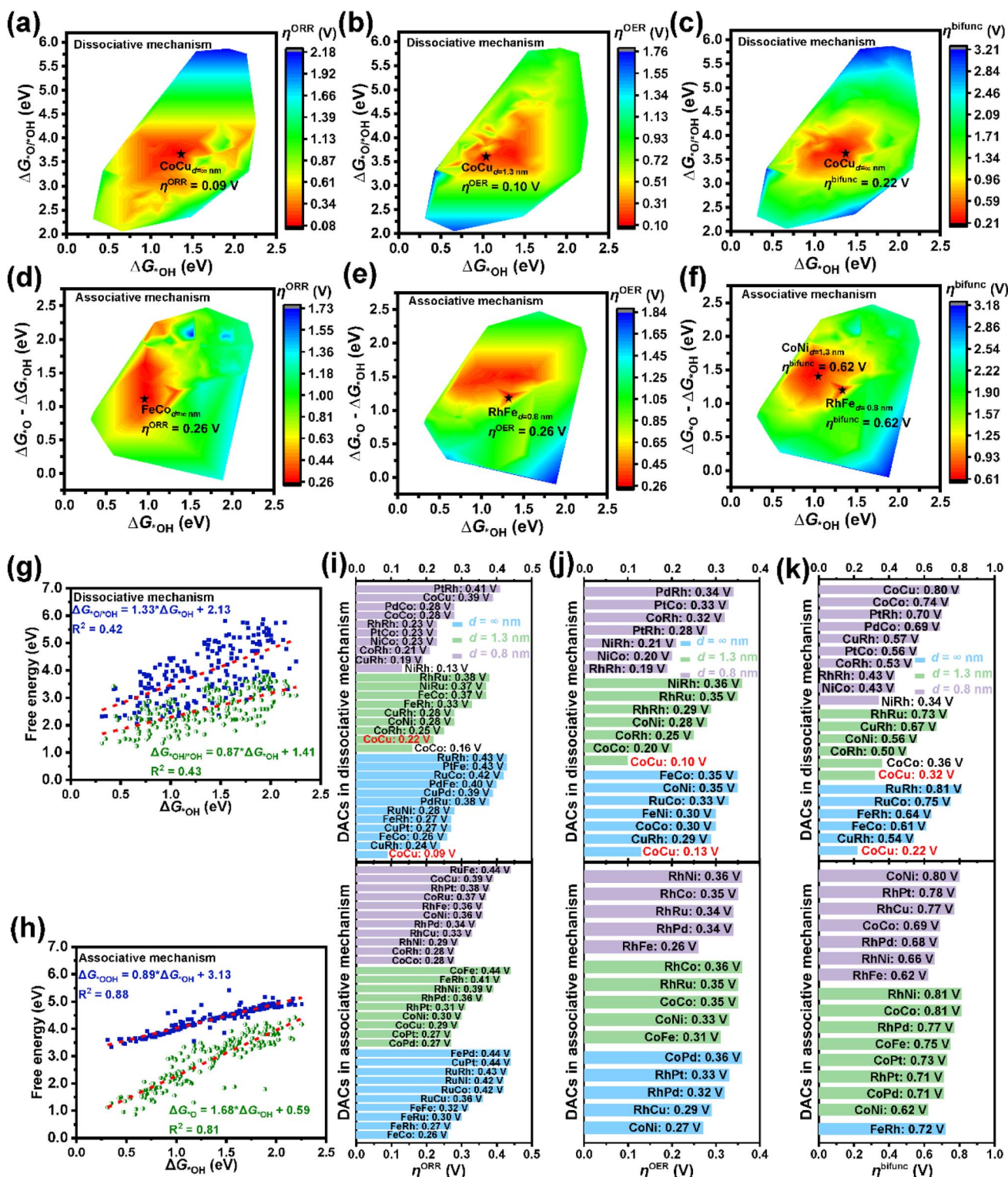This journal is © The Royal Society of Chemistry 2024

Fig. 3 Theoretical oxygen electrocatalyzing activity of DACs in this study. In the dissociative mechanism, ORR overpotential (a), OER over-potential (b), and bifunctional overpotential (c). In the associative mechanism, ORR overpotential (d), OER overpotential (e), and bifunctional overpotential (f). The stars in overpotential graphs indicate the DACs with the highest activity in this study. The fitting of Gibbs free energy between 3 intermediates in the dissociative mechanism (g) and associative mechanism (h). The red dashed lines represent the linear fitting of Gibbs free energy between intermediates. Potential DAC candidates with overpotential lower than the benchmarks for the ORR (i), OER (j), and bifunctional catalysis (k), respectively. The three benchmarks are 0.45 V, 0.37 V, and 0.82 V, respectively.
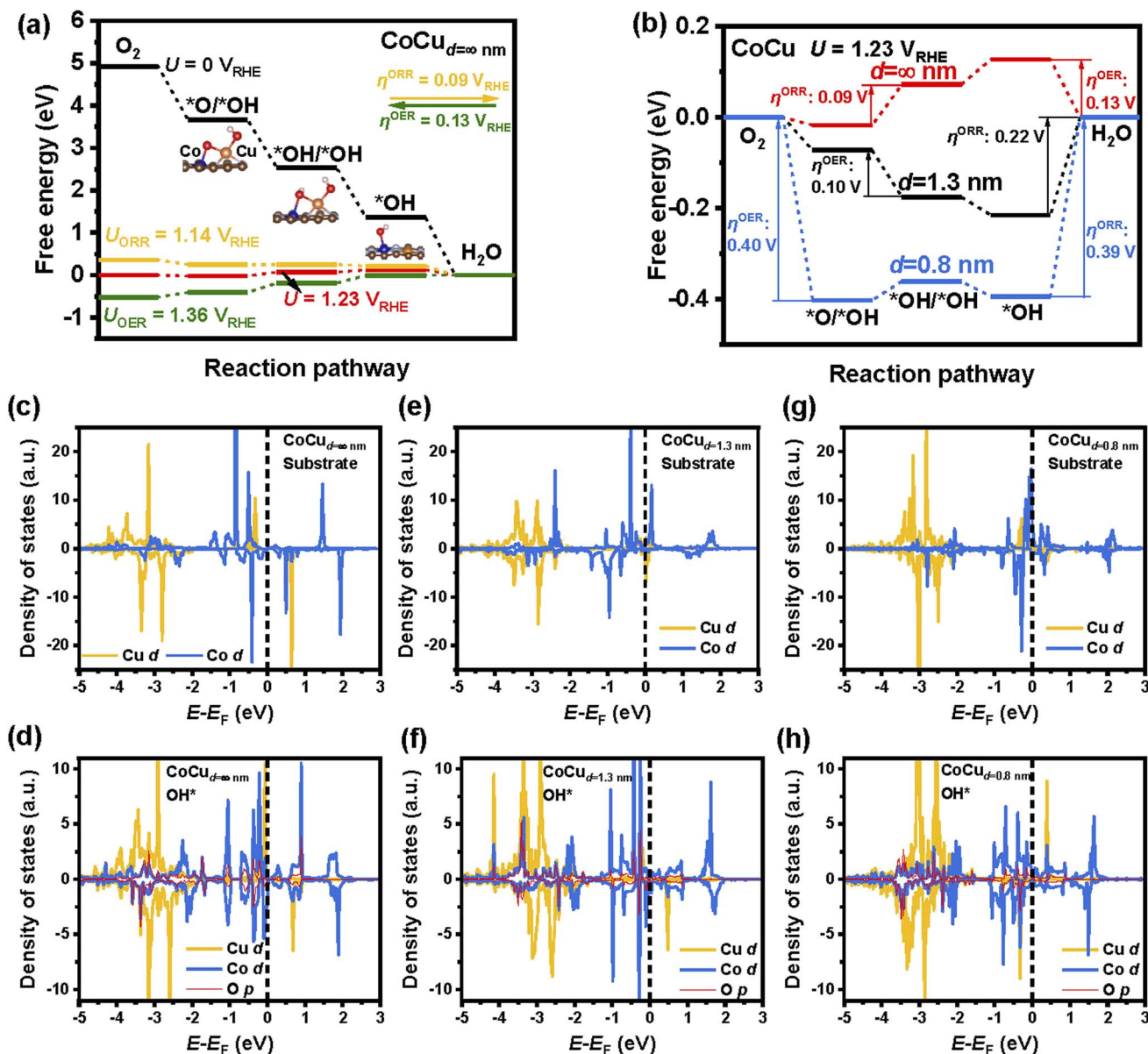
Fig. 4 Theoretical activity and electronic structures of CoCuN$_6$-DACs at different curvatures. (a) Gibbs free energy diagram for CoCuN$_6$-DACs in the planar state in the dissociative mechanism. The adsorption configurations of intermediates at each step are shown under the step. (b) Gibbs free energy diagram for CoCuN$_6$-DACs at different curvatures in the dissociative mechanism. The partial density of states (pDOS) of CoCuN$_6$-DACs without curvature before (c) and after (d) the adsorption of the OH intermediate. PDOS of CoCuN$_6$-DACs in 1.3 nm CNTs before (e) and after (f) the adsorption of the OH intermediate. PDOS of CoCuN$_6$-DACs in 0.8 nm CNTs before (g) and after (h) the adsorption of the OH intermediate. The black dashed line in pDOS represents the Fermi level.

with ΔG_{*OH} in a linear manner, with $R^2 > 0.8$, as shown in Fig. 3h. This demonstrates that the adsorption of intermediates in the associative mechanism conforms to the scaling relationship, which impedes finding of improved DAC candidates for oxygen-involving reactions.

Fig. 3i–k list the potential DACs under the three curvature conditions for the ORR, OER, and bifunctional oxygen electrocatalysis for both mechanisms. For the ORR, Fig. 3i showcases 31 potential candidates in the dissociative mechanism and 30 in the associative mechanism. Among these candidates, FeCo$_{d=\infty\ nm}$ exhibits excellent ORR activity in both mechanisms

($\eta^{ORR} = 0.26$ V), in line with experimental[65] and other theoretical[60] results, since the limiting step on this DAC in both mechanisms is *OH → H$_2$O. It should be noted that 4 candidates exhibit superior ORR activity in the dissociative mechanism with η^{ORR} below 0.2 eV:

- CoCu$_{d=\infty\ nm}$ (0.09 V),
- CoCo$_{d=1.3\ nm}$ (0.16 V),
- NiRh$_{d=0.8\ nm}$ (0.13 V),
- CuRh$_{d=0.8\ nm}$ (0.19 V).

For the OER, Fig. 3j exhibits 21 potential candidates in the dissociative mechanism and 15 in the associative mechanism.

28386 | J. Mater. Chem. A, 2024, 12, 28381–28389

This journal is © The Royal Society of Chemistry 2024

The CoNi$_{d=\infty\ nm}$-DAC is a promising OER catalyst in both mechanisms, especially in the associative mechanism (η^{OER} = 0.27 V), which is in line with the experimental result that atomically dispersed Co/Ni dual sites anchored on nitrogen-doped carbon exhibits a low η^{OER} of 0.25 V at 10 mA cm^{-2}.[66] We note here that 3 candidates exhibit superior ORR activity in the dissociative mechanism with η^{OER} below 0.2 eV:

- CoCu$_{d=\infty\ nm}$ (0.13 V),
- CoCu$_{d=1.3\ nm}$ (0.10 V), and
- RhRh$_{d=0.8\ nm}$ (0.19 V).

For bifunctional oxygen electrocatalysis, Fig. 3k lists 22 promising candidates in the dissociative mechanism and 16 in the associative mechanism. We note that 4 candidates exhibit superior ORR activity in the dissociative mechanism with η^{bifunc} below 0.4 eV:

- CoCu$_{d=\infty\ nm}$ (0.22 V),
- CoCu$_{d=1.3\ nm}$ (0.32 V),
- CoCo$_{d=1.3\ nm}$ (0.36 V), and
- NiRh$_{d=0.8\ nm}$ (0.34 V).

For both mechanisms, we found DACs with ORR/OER overpotential lower than 0.30 V, the theoretical minimum for SACs, suggesting the superiority of DACs over SACs for oxygen electrocatalysis. Our screening provides many candidates for mono- and bi-functional oxygen electrocatalysis in rechargeable metal–air batteries. The excellent candidates with low ORR overpotential can facilitate feasible discharging in rechargeable metal–air batteries, while those with low OER overpotential allow for smooth charging. And those with low bifunctional overpotential can act as bifunctional catalysts to accelerate reactions in discharging and charging cycles.

3.3. Oxygen electrocatalysis on CoCu DACs

In the planar state, the CoCuN$_6$-DAC exhibits superior activity for mono- and bi-functional oxygen electrocatalysis in the dissociative mechanism (η^{ORR} = 0.09 V, η^{OER} = 0.13 V, and η^{bifunc} = 0.22 V) as shown in Fig. 4a, which is much better than that of the CoN$_4$-SAC and CuN$_4$-SAC in both the associative and dissociative mechanisms as shown in Table S4.† This indicates the superiority of DACs for oxygen electrocatalysis over SACs. Moreover, for planar-state DACs, the activity of CoCuN$_6$ in the dissociative mechanism is better than that of CoCoN$_6$ and CuCuN$_6$ in both the associative and dissociative mechanisms as shown in Table S4,† which suggests that synergy between heterogeneous Co and Cu atoms is better than their homogeneous counterparts. In addition, the hydrogen adsorption free energy (ΔG_{*H}) on the planar-state CoCuN$_6$-DAC is 0.64 eV, indicating that HER activity on this DAC is quite low, making the HER an unlikely competitive reaction to the ORR.[67]

Three CoCuN$_6$-DACs were selected to understand the curvature effects on DACs for oxygen electrocatalysis in the dissociative mechanism based on the following two reasons: first, all three CoCu-DACs under different curvature conditions are potential candidates for bifunctional oxygen electrocatalysis as shown in Fig. 3k. Moreover, the CoCu$_{d=\infty\ nm}$-DAC (η^{ORR} = 0.09 V) and CoCu$_{d=1.3\ nm}$-DAC (η^{OER} = 0.10 V) are the optimal candidates for the ORR and OER, respectively. As shown in Fig. 4b and S4,† the adsorption free energies of all intermediates in the whole dissociative pathway gradually decrease with increasing curvature from $d = \infty$ nm to $d = 0.8$ nm, suggesting that the adsorption strength of these intermediates increases with curvature.[43] On the CoCu$_{d=\infty\ nm}$-DAC, the adsorption free energies of all intermediates are close to zero, leading to its superb activity for mono- and bi-functional oxygen electrocatalysis, with η^{ORR} = 0.09 V, η^{OER} = 0.13 V, and and η^{bifunc} = 0.22 V. The rate-limiting step for the ORR on the CoCu$_{d=\infty\ nm}$-DAC is *O + *OH → 2*OH, while that for the OER is H$_2$O → *OH. On the CoCu$_{d=1.3\ nm}$-DAC, η^{OER} is smaller while η^{ORR} and η^{bifunc} are larger than those on the CoCu$_{d=\infty\ nm}$-DAC, with η^{OER} = 0.10 V, η^{ORR} = 0.22 V, and η^{bifunc} = 0.32 V. The rate-limiting step for the ORR on the CoCu$_{d=1.3\ nm}$-DAC is *OH → H$_2$O, while that for the OER is 2*OH → *O/*OH. On CoCu$_{d=0.8\ nm}$, all three overpotentials are the largest among studied CoCuN$_6$-DACs, with η^{ORR} = 0.39 V, η^{OER} = 0.40 V, and η^{bifunc} = 0.80 V. The rate-limiting step for the ORR on the CoCu$_{d=0.8\ nm}$-DAC is *OH → H$_2$O, while that for the OER is *O/*OH → O$_2$.

To understand the electronic origin of the gradually strengthened adsorption on CoCuN$_6$-DACs with increasing curvature, the projected density of states (pDOS) of related atomic orbitals were compared before and after the adsorption of the OH intermediate, as shown in Fig. 4c–h. The OH intermediate is chosen for analysis of the electronic properties since it is the common intermediate in the two mechanisms. For three CoCu-DACs, main peaks of the p orbitals of O atoms overlap well with the d orbitals of Co atoms, suggesting that O atoms bond to Co atoms in the three systems, in line with the relaxed structures where O bonds with Co. Compared with the CoCu$_{d=\infty\ nm}$-DAC, the d orbitals of the Co atoms in the CoCu$_{d=1.3\ nm}$-DAC and CoCu$_{d=0.8\ nm}$-DAC have more electronic states near the Fermi level, which facilitates electron transfer between Co and O in DACs on CNT substrates, leading to stronger adsorption of *OH on the CoCu$_{d=1.3\ nm}$-DAC and CoCu$_{d=0.8nm}$-DAC. As for the d orbitals of the Cu atoms, the CoCu$_{d=1.3\ nm}$-DAC and CoCu$_{d=0.8\ nm}$-DAC also have more electronic states near the Fermi level than the CoCu$_{d=\infty\ nm}$-DAC. This allows stronger adsorption of *O/*OH and *2OH on two curved CoCu-DACs than planar CoCu$_{d=\infty\ nm}$-DAC, since adsorption of intermediates in these two steps involves both Co and Cu atoms.

4. Conclusion

Summarizing, we employed DFT calculations to investigate the stability and electrocatalytic activity for two mechanisms on curved DACs for mono- and bi-functional oxygen electrocatalysis. We found that all studied DACs have negative formation energies and positive dissolution potentials, suggesting their synthetic feasibility and electrochemical stability.

We found some promising catalysts with ultra-high predicted activity in the dissociative mechanism for both mono- and bi-functional oxygen electrocatalysis:

- CoCu$_{d=\infty\ nm}$-DAC (with η^{ORR} = 0.09 V, η^{OER} = 0.13 V, and η^{bifunc} = 0.22 V) and

This journal is © The Royal Society of Chemistry 2024

J. Mater. Chem. A, 2024, **12**, 28381–28389 | **28387**

• CoCu$_{d=1.3\text{ nm}}$-DAC (with $\eta^{\text{ORR}} = 0.22$ V, $\eta^{\text{OER}} = 0.10$ V, and $\eta^{\text{bifunc}} = 0.32$ V).

These studies suggest many potential candidates for oxygen electrocatalysis in rechargeable metal–air batteries, fuel cells, and electrolyzers.

In addition, we demonstrated that in the dissociative mechanism, the scaling relationship between intermediates in oxygen electrocatalysis on studied DACs is broken; while in the associative mechanism, this scaling relationship limits the DACs' activity. Traditionally, only the associative mechanism has usually been considered for oxygen electrocatalysis on dual-atom catalysts, with the possible synergy between two active sites neglected, which we show is an oversight. Thus, we show that for the dissociative mechanism, the synergy between two active sites can break the scaling relationship between intermediates in oxygen electrocatalysis, leading to catalysts with extremely high activity.

Moreover, we found that using CNTs to increase the curvature from $d = \infty$ nm to $d = 0.8$ nm, gradually strengthens the adsorption of all intermediates on CoCuN$_6$-DACs. By comparing the partial DOS around the Fermi level of related systems, we found that the enhanced adsorption occurs due to increased electronic states of metal atoms near the Fermi level.

Data availability

The data supporting this article have been included as part of the ESI.†

Conflicts of interest

The authors declare that they have no known competing financial interests or personal relationships that could have appeared to influence the work reported in this paper.

Acknowledgements

References

1 R. Cao, J.-S. Lee, M. Liu and J. Cho, *Adv. Energy Mater.*, 2012, **2**, 816–829.

2 C. Wei, R. R. Rao, J. Peng, B. Huang, I. E. L. Stephens, M. Risch, Z. J. Xu and Y. Shao-Horn, *Adv. Mater.*, 2019, **31**, 1806296.

3 J. Fu, Z. P. Cano, M. G. Park, A. Yu, M. Fowler and Z. Chen, *Adv. Mater.*, 2017, **29**, 1604685.

4 I. Katsounaros, S. Cherevko, A. R. Zeradjanin and K. J. J. Mayrhofer, *Angew. Chem., Int. Ed.*, 2014, **53**, 102–121.

5 K. Jiao, J. Xuan, Q. Du, Z. Bao, B. Xie, B. Wang, Y. Zhao, L. Fan, H. Wang, Z. Hou, S. Huo, N. P. Brandon, Y. Yin and M. D. Guiver, *Nature*, 2021, **595**, 361–369.

6 B. G. Pollet, S. S. Kocha and I. Staffell, *Curr. Opin. Electrochem.*, 2019, **16**, 90–95.

7 Y. Jiao, Y. Zheng, M. Jaroniec and S. Z. Qiao, *Chem. Soc. Rev.*, 2015, **44**, 2060–2086.

8 J. Wu and H. Yang, *Acc. Chem. Res.*, 2013, **46**, 1848–1857.

9 M. Escudero-Escribano, P. Malacrida, M. H. Hansen, U. G. Vej-Hansen, A. Velázquez-Palenzuela, V. Tripkovic, J. Schiøtz, J. Rossmeisl, I. E. L. Stephens and I. Chorkendorff, *Science*, 2016, **352**, 73–76.

10 J. H. Montoya, L. C. Seitz, P. Chakthranont, A. Vojvodic, T. F. Jaramillo and J. K. Nørskov, *Nat. Mater.*, 2017, **16**, 70–81.

11 Y. Lee, J. Suntivich, K. J. May, E. E. Perry and Y. Shao-Horn, *J. Phys. Chem. Lett.*, 2012, **3**, 399–404.

12 A. Wang, J. Li and T. Zhang, *Nat. Rev. Chem*, 2018, **2**, 65–81.

13 S. Mitchell and J. Pérez-Ramírez, *Nat. Commun.*, 2020, **11**, 4302.

14 C. Zhu, S. Fu, Q. Shi, D. Du and Y. Lin, *Angew. Chem., Int. Ed.*, 2017, **56**, 13944–13960.

15 Y. Wang, D. Wang and Y. Li, *Adv. Mater.*, 2021, **33**, 2008151.

16 Q. Zhang and J. Guan, *Adv. Funct. Mater.*, 2020, **30**, 2000768.

17 A. Wang, J. Li and T. Zhang, *Nat. Rev. Chem*, 2018, **2**, 65–81.

18 S. Mitchell and J. Pérez-Ramírez, *Nat. Commun.*, 2020, **11**, 4302.

19 R. Li and D. Wang, *Adv. Energy Mater.*, 2022, **12**, 2103564.

20 M. Tamtaji, M. G. Kim, Z. Li, S. Cai, J. WANG, P. R. Galligan, F.-F. Hung, H. Guo, S. Chen, Z. Luo, W. Wu, W. A. Goddard and G. Chen, *Nano Energy*, 2024, 109634.

21 H. Shang, X. Zhou, J. Dong, A. Li, X. Zhao, Q. Liu, Y. Lin, J. Pei, Z. Li, Z. Jiang, D. Zhou, L. Zheng, Y. Wang, J. Zhou, Z. Yang, R. Cao, R. Sarangi, T. Sun, X. Yang, X. Zheng, W. Yan, Z. Zhuang, J. Li, W. Chen, D. Wang, J. Zhang and Y. Li, *Nat. Commun.*, 2020, **11**, 3049.

22 L. Peng, L. Shang, T. Zhang and G. I. N. Waterhouse, *Adv. Energy Mater.*, 2020, **10**, 2003018.

23 C. Wan, X. Duan and Y. Huang, *Adv. Energy Mater.*, 2020, **10**, 1903815.

24 J. Zhang, H. Yang and B. Liu, *Adv. Energy Mater.*, 2021, **11**, 2002473.

25 Y. Li, Y. Feng, D. Zheng, X. Zhao, Y. Zhou, X. Fu and X. Chen, *Chem. Eng. J.*, 2023, **476**, 146753.

26 M. Tamtaji, M. G. Kim, J. WANG, P. R. Galligan, H. Zhu, F.-F. Hung, Z. Xu, Y. Zhu, Z. Luo, W. A. Goddard and G. Chen, *Advanced Science*, 2024, 2309883.

27 Y. Pang, C. Su, L. Xu and Z. Shao, *Prog. Mater. Sci.*, 2023, **132**, 101044.

28 M. Li, H. Wang, W. Luo, P. C. Sherrell, J. Chen and J. Yang, *Adv. Mater.*, 2020, **32**, 2001848.

29 T. Wang, Q. Zhao, Y. Fu, C. Lei, B. Yang, Z. Li, L. Lei, G. Wu and Y. Hou, *Small Methods*, 2019, **3**, 1900210.

30 Y. Wang, Y. Liu, W. Liu, J. Wu, Q. Li, Q. Feng, Z. Chen, X. Xiong, D. Wang and Y. Lei, *Energy Environ. Sci.*, 2020, **13**, 4609–4624.

31 Y. Chen, J. Lin, Q. Pan, X. Liu, T. Ma and X. Wang, *Angew. Chem., Int. Ed.*, 2023, **62**, e202306469.

32 R. Li and D. Wang, *Adv. Energy Mater.*, 2022, **12**, 2103564.

28388 | *J. Mater. Chem. A*, 2024, **12**, 28381–28389

This journal is © The Royal Society of Chemistry 2024

33 Y. Ying, X. Luo, J. Qiao and H. Huang, *Adv. Funct. Mater.*, 2021, **31**, 2007423.

34 C. Fang, J. Zhou, L. Zhang, W. Wan, Y. Ding and X. Sun, *Nat. Commun.*, 2023, **14**, 4449.

35 L. Zhao, S. Guo, H. Liu, H. Zhu, S. Yuan and W. Guo, *ACS Appl. Nano Mater.*, 2018, **1**, 6258–6268.

36 Q. Xu, H. Li, Y. Shi, Z. Bi and Y. Wu, *ACS Appl. Nano Mater.*, 2021, **4**, 600–611.

37 H. Liu, L. Zhao, Y. Liu, J. Xu, H. Zhu and W. Guo, *Catal. Sci. Technol.*, 2019, **9**, 5301–5314.

38 S. Yuan, G. Meng, D. Liu, W. Zhao, H. Zhu, Y. Chi, H. Ren and W. Guo, *ACS Appl. Mater. Interfaces*, 2022, **14**, 52544–52552.

39 W. Liu, K. Guo, Y. Xie, S. Liu, L. Chen and J. Xu, *Sci. Rep.*, 2023, **13**, 9926.

40 G. Han, X. Zhang, W. Liu, Q. Zhang, Z. Wang, J. Cheng, T. Yao, L. Gu, C. Du, Y. Gao and G. Yin, *Nat. Commun.*, 2021, **12**, 6335.

41 X. Zhou, Z. Jin, J. Zhang, K. Hu, S. Liu, H.-J. Qiu and X. Lin, *Nanoscale*, 2023, **15**, 2276–2284.

42 J. Wang, N. Li, Y. Jiang, H. Sheng and M. Sun, *Appl. Surf. Sci.*, 2024, **658**, 159858.

43 R. Cepitis, N. Kongi, J. Rossmeisl and V. Ivaništšev, *ACS Energy Lett.*, 2023, **8**, 1330–1335.

44 J. Liu, H. Xu, J. Zhu and D. Cheng, *JACS Au*, 2023, **3**, 3031–3044.

45 J. P. Perdew, K. Burke and M. Ernzerhof, *Phys. Rev. Lett.*, 1996, **77**, 3865–3868.

46 G. Kresse and J. Furthmüller, *Comput. Mater. Sci.*, 1996, **6**, 15–50.

47 G. Kresse and J. Furthmüller, *Phys. Rev. B*, 1996, **54**, 11169–11186.

48 G. Kresse and D. Joubert, *Phys. Rev. B*, 1999, **59**, 1758–1775.

49 S. Grimme, *J. Comput. Chem.*, 2006, **27**, 1787–1799.

50 S. Grimme, J. Antony, S. Ehrlich and H. Krieg, *J. Chem. Phys.*, 2010, **132**, 154104.

51 K. Mathew, R. Sundararaman, K. Letchworth-Weaver, T. A. Arias and R. G. Hennig, *J. Chem. Phys.*, 2014, **140**, 084106.

52 K. Mathew, V. S. C. Kolluru, S. Mula, S. N. Steinmann and R. G. Hennig, *J. Chem. Phys.*, 2019, **151**, 234101.

53 A. Cao and J. K. Nørskov, *ACS Catal.*, 2023, **13**, 3456–3462.

54 J. K. Nørskov, J. Rossmeisl, A. Logadottir, L. Lindqvist, J. R. Kitchin, T. Bligaard and H. Jónsson, *J. Phys. Chem. B*, 2004, **108**, 17886–17892.

55 M. Tamtaji, Q. Peng, T. Liu, X. Zhao, Z. Xu, P. R. Galligan, M. D. Hossain, Z. Liu, H. Wong, H. Liu, K. Amine, Y. Zhu, W. A. Goddard III, W. Wu and Z. Luo, *Nano Energy*, 2023, **108**, 108218.

56 J. Wang, Z. Huang, W. Liu, C. Chang, H. Tang, Z. Li, W. Chen, C. Jia, T. Yao, S. Wei, Y. Wu and Y. Li, *J. Am. Chem. Soc.*, 2017, **139**, 17281–17284.

57 X.-M. Liang, H.-J. Wang, C. Zhang, D.-C. Zhong and T.-B. Lu, *Appl. Catal., B*, 2023, **322**, 122073.

58 L.-L. Liu, M. ul Haq, L. Zhang, J.-J. Feng, L. Wu and A.-J. Wang, *J. Electroanal. Chem.*, 2023, **951**, 117953.

59 J. Wang, W. Liu, G. Luo, Z. Li, C. Zhao, H. Zhang, M. Zhu, Q. Xu, X. Wang, C. Zhao, Y. Qu, Z. Yang, T. Yao, Y. Li, Y. Lin, Y. Wu and Y. Li, *Energy Environ. Sci.*, 2018, **11**, 3375–3379.

60 Y. Meng, C. Yin, K. Li, H. Tang, Y. Wang and Z. Wu, *ACS Sustain. Chem. Eng.*, 2019, **7**, 17273–17281.

61 Y. Meng, Y. Gao, K. Li, H. Tang, Y. Wang and Z. Wu, *J. Phys. Chem. C*, 2020, **124**, 9142–9150.

62 Y. Meng, C. Yin, K. Li, H. Tang, Y. Wang and Z. Wu, *ACS Sustain. Chem. Eng.*, 2019, **7**, 17273–17281.

63 F. Rehman, S. Kwon, C. B. Musgrave, M. Tamtaji, W. A. Goddard and Z. Luo, *Nano Energy*, 2022, **103**, 107866.

64 J. Pérez-Ramírez and N. López, *Nat. Catal.*, 2019, **2**, 971–976.

65 J. Wang, Z. Huang, W. Liu, C. Chang, H. Tang, Z. Li, W. Chen, C. Jia, T. Yao, S. Wei, Y. Wu and Y. Li, *J. Am. Chem. Soc.*, 2017, **139**, 17281–17284.

66 Z. Pei, X. F. Lu, H. Zhang, Y. Li, D. Luan and X. W. (David) Lou, *Angew. Chem., Int. Ed.*, 2022, **61**, e202207537.

67 M. Tamtaji, Y. Li, Y. Cai, H. Liu, W. A. Goddard III and G. Chen, *J. Mater. Chem. A*, 2023, **11**, 25410–25421.

This journal is © The Royal Society of Chemistry 2024

J. Mater. Chem. A, 2024, **12**, 28381–28389 | **28389**